Cement and Concrete Composites 136 (2023) 104888

Contents lists available at ScienceDirect

Cement and Concrete Composites

journal homepage: www.elsevier.com/locate/cemconcomp

Reducing carbonation degradation and enhancing elastic properties of calcium silicate hydrates using biomimetic molecules

Muhammad Intesarul Haque [a], Ishrat Baki Borno [a], Rakibul I. Khan [b], Warda Ashraf [a,*]

[a] Department of Civil Engineering, University of Texas at Arlington, Nedderman Hall, Arlington, TX, 76010, USA
[b] Laticrete International Inc., Bethany, CT 06524-3423, USA

ARTICLE INFO

Keywords:
CSH
Polydopamine
L-aspartic acid
Carbonation
Polymerization

ABSTRACT

This study presents a novel way of reducing the carbonation-induced degradation of CSH using organic molecules. Synthetic CSH batches were prepared with the addition of L-aspartic acid and polydopamine. The effects of these molecules on the synthesized CSH before and after carbonation were monitored using various experimental techniques, including ^{29}Si NMR, TEM, nanoindentation, and FTIR. It was observed that, without the presence of biomimetic molecules, CSH was converted to a fully polymerized silica gel after 168 h of carbonation, as evident by the presence of Q^3 and Q^4 species in ^{29}Si NMR spectra. On the other hand, biomimetic molecules modified CSH retained the original chain-like arrangements even after 28 days of carbonation, as identified by the presence of Q^1 and Q^2 species in ^{29}Si NMR spectra. Additionally, the biomimetic molecules modification increased the elastic modulus of CSH by 3–9 times, which were further increased upon carbonation.

1. Introduction

Concrete produced using a high volume of supplementary cementitious materials (SCMs) and Ca-rich alkali-activated materials are sustainable alternatives to ordinary Portland cement (OPC)-based materials due to their lower carbon footprint [1,2]. Those sustainable cementitious materials primarily contain CSH (or C-A-S-H) as the binding phases and are devoid of $Ca(OH)_2$. Because of the absence of $Ca(OH)_2$, the CSH present in those composites is more readily damaged by atmospheric CO_2 compared to the OPC [3–9]. In hardened cementitious composites, CO_2 can diffuse into the empty pores, where it reacts with water from the pore solution and forms bicarbonate ions. The bicarbonate ions react with portlandite ($Ca(OH)_2$) and CSH, forming $CaCO_3$ and water. The reaction between CO_2 present in atmosphere with CSH results in decalcification and polymerization of the binding phases followed by the formation of calcite [10]. The low molecular volume of calcite compared to that of CSH eventually leads to increased porosity in the matrix [7,11–13] in addition to lower compressive strengths [14], carbonation shrinkage [15,16], and increased vulnerability of reinforcement to corrosion due to the reduction of alkalinity [17,18]. The increase in large porosity in the cementitious matrixes due to carbonation also increases the diffusivity of detrimental chloride/sulfate ions into the matrix, resulting in the further degradation of the durability performances of the matrix [19–21].

One of the potential solutions for reducing the extent of carbonation damage in cementitious materials is to control the polymorphs of the precipitated $CaCO_3$ particles [22]. Calcite, aragonite, vaterite, and amorphous calcium carbonate (ACC) are the primary polymorphs that can form during the carbonation of cementitious matrixes containing CSH or C-A-S-H as the primary binding phases [23–25]. Other crystalline polymorphs, including ikaite ($CaCO_3 \bullet 6H_2O$) and monohydrocalcite ($CaCO_3 \bullet H_2O$), may also form [26,27], but these are very rare. Even though this polymorph selection route is affected by several factors, including relative humidity (RH) [28], CO_2 concentration [29], and pH [30], in general, the final polymorph is calcite as it is the most stable form of $CaCO_3$. However, these polymorphs have different intrinsic characteristics, including solubility. The solubility constants for calcite, aragonite, and vaterite are $10^{-8.48}$,$10^{-8.34}$ and $10^{-7.91}$, respectively [31,32], and ACC is 120 times more soluble than calcite [33]. As suggested by Morandeau and White [22], the formation of ACC can reduce the extent of carbonation in cementitious matrixes due to the higher solubility of this phase and consequent saturation of solution. In support of this, a few recent studies have also shown that magnesium-stabilized ACC formation can lead to lower carbonation damage in alkali activated materials (AAM) [22,34].

An alternative method of controlling the crystallization of $CaCO_3$ can

---

* Corresponding author.
E-mail address: warda.ashraf@uta.edu (W. Ashraf).

https://doi.org/10.1016/j.cemconcomp.2022.104888
Received 15 May 2022; Received in revised form 24 November 2022; Accepted 1 December 2022
Available online 5 December 2022

be learned by studying the natural biomineralization process [35]. A series of biomimetic molecules have already been identified that can stabilize typically metastable ACC, aragonite, and vaterite during the biomineralization process by forming organic-inorganic hybrids [36–39]. However, the effectiveness of those biomimetic molecules in cementitious environments to control the crystallization of $CaCO_3$ is not well studied yet. In our previous study, we observed that a few amino acids can control the crystallization of $CaCO_3$ in carbonation-cured wollastonite composites [40]. Among the tested amino acids, L-aspartic acid (L-Asp) was found to stabilize ACC in carbonated composites. Such stabilization of ACC resulted in a reduced degree of carbonation, as expected, but also significantly improved mechanical performances of the carbonated composite [40]. The improved mechanical performance was attributed to the formation of organic-inorganic hybrid phases [40]. Additionally, several past studies suggested that polydopamine (PDA) can be used to control the crystallization of $CaCO_3$, and stabilize vaterite and ACC [41–44,55]. The additional benefit of PDA is its self-adhesive characteristics that results from its polymerization in an alkaline environment [44]. Because of these adhesive characteristics, Fang et al. applied PDA in fine sand to improve its adherence to cement particles [46]. Due to the ability of L-Asp and PDA to mimic biomineralization processes, these molecules are referred to as the biomimetic molecules for the remainder of this study.

The presented study explored the role of the above-mentioned molecules, including L-Asp and PDA, to control the crystallization of $CaCO_3$ during the carbonation of the CSH. It is worth noting that synthesis of CSH modified with biomimetic molecules has been attempted in the past. Picker et al. [47] studied the adsorption of peptides on CSH with different calcium to silica (C/S) ratios to investigate the possible interactions between CSH and peptides. They revealed the role of various functional groups of peptides on interaction with CSH. According to the authors, an organic additive should contain OH-forming and hydrophobic functional groups to adsorb strongly on CSH. This suggests that a biomimetic molecule with an ability to interact with other molecules through different functional groups can be considered a promising organic compound for manipulating the properties of CSH. A study by Kamali and Ghahremaninezhad [48] further showed that such organic-inorganic hybrids can be produced in cementitious materials by forming composites containing CSH and organic biomolecules. Specifically, the authors have used amino acids and proteins to modify the atomic structure of CSH, resulting in a decrease of the Young's modulus [48].

The primary goal of this study was to evaluate the effectiveness of the selected biomimetic molecules to resist atmospheric carbonation degradation of CSH. To achieve this goal, L-Asp and PDA were used in the synthesis of CSH by following the same approach of producing organic-polymer modified CSH [49,50]. A series of micro-to-nano scale experimental techniques were then used to investigate the effects of the biomimetic molecules on nanoscale characteristics of CSH before carbonation and monitor the phase evolution during the carbonation. The specific research objectives of this study are: (i) to investigate the effects of biomimetic molecules if they can reduce or prevent carbonation degradation of CSH by forming the metastable calcium carbonates (i.e., vaterite and ACC), (ii) to understand how biomimetic molecules can play a role to enhance the elastic properties of CSH.

2. Materials and methods

2.1. Raw materials

Commercially available calcium nitrate ($Ca(NO_3)_2$•$4H_2O$) and sodium silicate (Na_2SiO_3•$9H_2O$) were used as the raw ingredients to synthesize pure CSH. For synthesizing biomimetic molecule-modified CSH, high purity grade L-aspartic acid (L-Asp) and dopamine hydrochloride ($C_{18}H_{11}NO_2$•HCl, 99% purity; addressed as dopamine in this study) were purchased from VWR International (Pennsylvania, USA). The molar mass of L-aspartic acid and dopamine hydrochloride were 133.10 g/mol and 189.64 g/mol. Fig. 1 displays the schematic drawing of the CSH structure and the molecular structures of L-aspartic acid and dopamine.

2.2. CSH synthesis

Previously published studies [49] were followed to synthesize pure and biomimetic molecule-modified CSH. For the pure CSH preparation, at first, 250 ml deionized water was poured into a beaker. The water was boiled to get rid of the air bubbles and dissolved CO_2 gas. Next, the temperature of the solution was lowered to 50 °C. Sodium hydroxide (NaOH) was then added to the water to increase the pH to 11.5. After that, 10 g of calcium nitrate salt was dissolved in the water. Meanwhile, sodium silicate salt was dissolved in 250 ml of deionized water and poured in a separate beaker. The amount of sodium silicate salt was calculated based on the calcium to silica (C/S) ratio of 1.5. Next, the calcium nitrate solution beaker was placed on the hotplate magnetic stirrer. The stirrer was rotated at 450 rpm and the temperature was set at 50 °C. After that, the sodium silicate solution was added drop by drop to the calcium nitrate solution with a burette. Once the addition of sodium silicate solution was done, the beaker was kept on the hotplate magnetic stirrer, maintaining the same rotation and temperature for 48 h. After 48 h, the CSH gel was filtered and then put inside the oven at 50 °C for 24 h. After that, the CSH gel was dried and formed solid chunks. The chunks were ground using mortar-and-pestle. All the above activities were performed in a nitrogen gas purging environment to avoid carbonation degradation of the synthesized CSH. Fig. 2 shows the different steps of CSH preparation.

A 10% dosage (by weight percentage of CSH) of L-Asp and PDA was chosen for the biomimetic molecules modified CSH preparation. This 10% dose was selected based on our preliminary study using portlandite carbonation. In this case, biomimetic molecules were added to the boiled pH 11.5 water, prior to adding the calcium nitrate salt. The solution was mixed for approximately 2 min to ensure the biomimetic molecules were visibly dissolved in the solution. After that, the calcium nitrate salt was added to the solution. All other steps remained the same as those for the pure CSH. Worth noting, both pure CSH and L-Asp modified CSH had a whitish color (Fig. 2(f)). However, the PDA modified CSH had darkish color (Fig. 2(f)). The conversion of dopamine hydrochloride to PDA is known to be responsible for the dark grey appearance [46]. Dopamine hydrochloride is soluble in water.

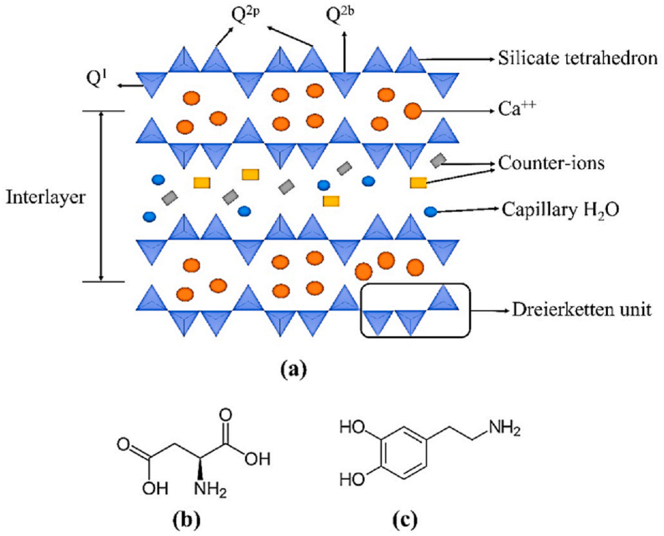

Fig. 1. (a) schematic CSH structure; (b) molecular structure of L-aspartic acid, and (c) molecular structure of dopamine (p: paring, b: bridging).

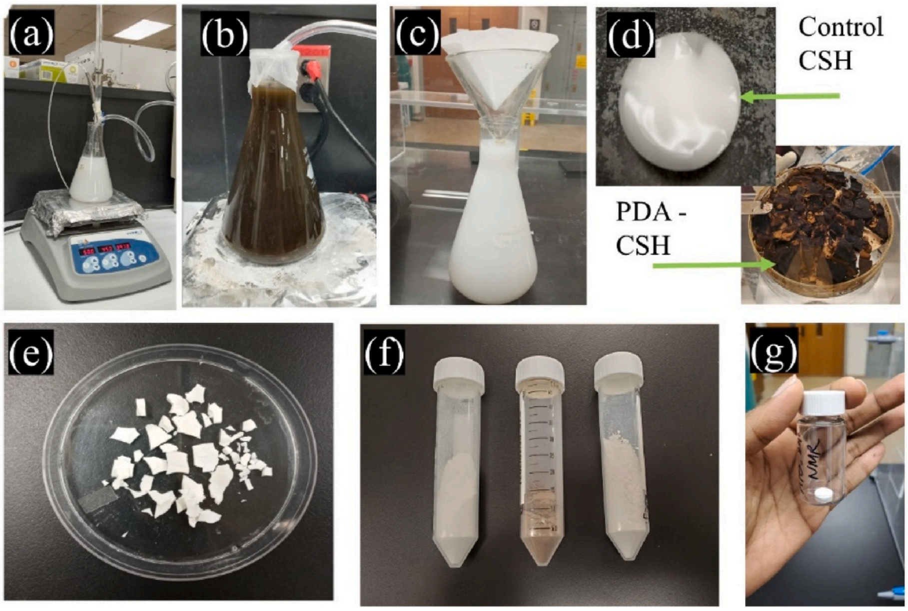

Fig. 2. (a) Sodium silicate solution being added to calcium nitrate solution with burette; (b) calcium nitrate and sodium silicate solution kept on hotplate for 48 h; (c) filtering out the CSH gel; (d) CSH gel (e) oven dried CSH; (f) ground synthetic CSH (from left: pure CSH, PDA modified CSH and L-Asp modified CSH); (g) prepared pellet (see Sec 2.3).

Dopamine tends to self-polymerize into polydopamine when the pH reaches around 8.5 [46,54,55].

From X-ray fluorescence (XRF) analysis, it was found that the C/S was around 1.0 for the prepared samples (Table 1). A lower C/S ratio than the target value was expected, considering the synthesis reaction is not 100% efficient.

2.3. Sample preparation

The obtained pure and modified CSH as per section 2.2 were in powder form. These powders were used to prepare pellets of approximately 2 mm thickness and 10 mm diameter using a pellet press by applying a 5 MPa load. These pellet CSH samples were then subjected to accelerated carbonation using a commercially available carbonation chamber. The chamber was operated to maintain a 4% CO_2 concentration at 27 °C and 75% relative humidity (RH). The pellet samples were extracted from the carbonation chamber after certain intervals as listed in Table 2. Since most of the characterization tests required powder samples, the collected carbonated pellets were ground using a mortar-and-pestle inside a glove box. The collected powder samples were preserved inside a vacuum chamber, ensuring an airtight environment and maintaining 11% RH controlled by a LiCl salt solution. Table 2 presents the test matrix for the various carbonation durations of the CSH pellets. As observed, the actual C/S ratios were lower than the target 1.5. Such reduced C/S ratios were expected as the efficiency of the CSH synthesis approach is not 100%.

2.4. Experimental methods

2.4.1. Transmission electron microscopy (TEM)

For TEM images, the CSH (either immediately after synthesizing or carbonated) powder was dispersed into an isopropanol solution. The solution was then ultrasonicated for 10 min using a commercially available sonicator (Cole-Parmer 8890). The samples were placed on a lacey carbon 300 mesh gold grid (Ted Pella Inc, USA) using a dropper. The images were collected using a Hitachi H-9500 transmission electron microscope and the operating voltage was 300 kV.

Table 1
XRF measurements for C/S = 1.5 samples.

	Control CSH	PDA – CSH	L-Asp – CSH
XRF measurements	1.0	0.9	0.9

Table 2
Matrix of experiments before and after carbonation of the samples.

Tests	Carbonation duration
Transmission Electron Microscopy (TEM)	0 h, 168 h
Thermogravimetric analysis with mass spectroscopy (TGA-MS)	168 h, 28 days
Nuclear Magnetic Resonance (NMR)	0 h, 168 h, 28 days
Fourier Transform Infrared Spectroscopy (FTIR)	0 h, 6 h, 24 h, 72 h, 168 h, 28 days
Nanoindentation	0 h, 168 h, 28 days
Scanning electron microscopy (SEM)	168 h, 28 days
X-Ray diffractions (XRD)	0 h, 28 days

2.4.2. Nuclear magnetic resonance (NMR)

Solid state magic angle spinning nuclear magnetic resonance was performed on the samples to characterize the local atomic structure of ^{29}Si. The NMR test was performed on 0 h, 24 h and 168 h carbonated samples. All the ^{29}Si solid-state NMR experiments were conducted at 7.05 T on a Varian Unity Inova 300 MHz spectrometer at the SCS NMR Facility of the University of Illinois at Urbana-Champaign, operating at a resonance frequency of ν_0 (^{29}Si) = 59.6 MHz, at room temperature. A Varian/Chemagnetics 7.5 mm double-resonance APEX HX magic-angle spinning (MAS) probe was used for all MAS experiments under a spinning rate of 4 kHz and TPPM 1H decoupling. All samples were finely ground and packed into 4 mm o. d. Standard zirconia rotors (typically around 210–580 mg). Experimental silicon chemical shift referencing, pulse calibration and setup were done using powdered octakis (trimethylsiloxy) silsesquioxane (Q8M8), which has a chemical shift of 11.45 ppm, relative to the primary standard, TMS at 0 ppm. The ^{29}Si pulse width used was 1.5 μs, corresponding to a 45-degree pulse. A recycle delay of 30 s was used and 1920 scans were acquired for each sample.

2.4.3. Fourier transform infrared spectroscopy (FTIR)

The Fourier-Transformed Infrared (FTIR) spectra of the powder samples were collected using the Attenuated Total Reflection (ATR) mode with 4 cm^{-1} resolution and 32 scans for each sample. Signal to noise ratio was lower than 3:1. FTIR test was conducted on 0 h, 6 h, 24 h, 72 h, 168 h and 28 days carbonated samples.

2.4.4. *Thermogravimetric analysis with mass spectroscopy (TGA-MS)*

TGA was coupled with a mass spectrometer (MS) for 168 h and 28 days carbonated samples. This coupled TGA-MS system enabled the separation and identification of any volatile elements coming off the sample during the heating process. In this case, TGA was performed using a Netzsch STA 449 F3 Jupiter Simultaneous Thermal Analysis (STA) instrument. All samples were measured under ultra-high purity helium gas (flow of 50 ml/min). The temperature was increased at a rate of 10 °C/min, and gases were transferred to the GC/MS instrumentation via a heated (250 °C) transfer line. An Agilent Technologies 7890A GC system equipped with a non-polar capillary column (Agilent J&B HP-5 packed with [5%-Phenyl-methylpolysiloxane]) coupled with a 5975 MSD spectrometer was used for the analyses of the gases released from the samples. A gas injection was triggered every minute (60 s) from the beginning of the heating cycle, and 0.25 ml of gas was sampled from the gases released by the compound and carrier gas (He).

2.4.5. *Nanoindentation*

For grid nanoindentation, 0 h, 168 h and 28 days carbonated samples were chosen. Because of the mirror like finishing of the pellet press die set, the CSH pellets could be used for nanoindentation measurements without any further surface preparation of the samples. The load function had three segments: (i) loading from zero to maximum load in the span of 5 s, (ii) holding at the maximum load for 5 s, (iii) unloading from maximum to zero load within 5 s. Since the depth of the indentations should also be small enough to determine the mechanical properties of the individual microscopic phases (i.e. indentation depth ≪ characteristic size of each microscopic phases) [56], a maximum of 300 μ-N force was selected for the SNI technique during this study. The average indentation depth for this load function was around 100–300 nm for a 30 μm × 30 μm area. The elastic moduli were determined from the load-depth plots using the Oliver and Pharr method [57]. Nanoindentation tests were performed using a Hysitron Triboindenter UB1 system (Hysitron Inc. Minneapolis, USA) fitted with a Berkovich diamond indenter probe. The tip area function was calibrated by performing several indents with various contact depths on a standard fused quartz sample. In all cases, a surface RMS roughness lower than 80 nm (measured with the Berkovich tip) was detected over an area of 60 μm × 60 μm.

2.4.6. *Scanning electron microscopy (SEM)*

The microstructures of 168 h and 28 days carbonated samples were evaluated using a Hitachi S4800 II FE-SEM. The instrument was operated in high vacuum mode with a 30 kV accelerated voltage and a working distance of about 10 mm. The cement paste sample was coated with platinum (Pt) before capturing the SEM images.

2.4.7. *X-ray diffractions (XRD)*

X-ray diffraction patterns of the paste samples were collected with a Bruker D-500 spectrometer using Cu Kα radiation (40 kV, 30 mA). Diffraction patterns were obtained for a 2θ range of 5°–60° with a step size of 0.03 (2θ) per second. XRD patterns were only obtained to ensure the quality of the synthesized CSH, and the patterns are provided in supplementary plots Figure S1 and Figure S2.

3. Results and discussion

3.1. *Characteristics of biomimetic molecules modified CSH*

3.1.1. *^{29}Si NMR spectra of pure and polymer-modified CSH*

The chemical environment of ^{29}Si is generally expressed as Q^n in silicate minerals, where Q denotes the silicon atom bonded tetrahedrally to four oxygen atoms and the superscript n refers to the number of the other $[SiO_4]^{4-}$ attached to the SiO_4 tetrahedron being investigated [58, 59]. Fig. 3 represents the ^{29}Si NMR spectra of the freshly prepared pure CSH and biopolymer-modified CSH. Based on the literature [60,61], the ^{29}Si NMR peaks were assigned as below: end groups and dimers (Q^1): −79.7 ppm; the bridging sites (Q^2_b): −82 pp; and pairing sites (Q^2_p): −85 ppm. The pure CSH was found to contain a relatively high intensity of Q^2 compared to that of Q^1. Such a high Q^2/Q^1 ratio is expected for CSH synthesized with a low C/S ratio [60]. As observed from the XRF measurements (Table 1), the actual C/S ratios of the synthesized samples were lower than the target ratio of 1.5, thus resulting in relatively high intensity for Q^2 in all the CSH samples. In the PDA modification, the intensities for Q^1 and Q^3 present in the CSH were increased. Therefore, the addition of PDA increased the non-uniformity in CSH structure. The effects of L-Asp addition were similar to those of PDA. Additionally, the L-Asp modified CSH showed the highest intensity of Q^0 species.

3.1.2. *Nanostructure of synthesized CSH*

Fig. 4 shows the TEM images of the pure CSH and biomimetic-molecule modified CSH nanostructures. The images were taken at two different magnification levels: 100 nm and 50 nm. Pure CSH was found to have lath or globule-like structure (Fig. 4(a) and (b)). Such morphology of CSH matches previous observations [62]. Interestingly, the addition of biomimetic molecules had distinct effects on the morphology of the CSH. The synthetic CSH with 10% PDA showed a foil-like morphology (Fig. 4(e) and (f)). Additionally, the CSH deposition appeared to have become denser due to the addition of PDA. Such an effect was more prominent in the case of the L-Asp modified CSH. Specifically; the TEM image of the L-Asp modified CSH showed the formation of randomly oriented needle-like shapes (Fig. 4(c) and (d)). The molecules interacted differently due to different chain length and charges. The PDA has longer chain length than the L-Asp (Fig. 1).

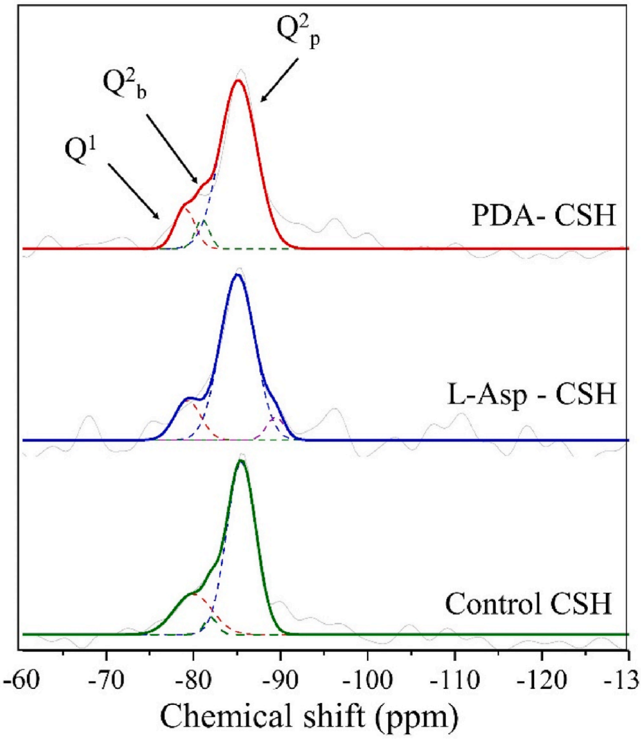

Fig. 3. ^{29}Si MAS NMR spectra of pure and modified CSH at 0 h carbonation period.

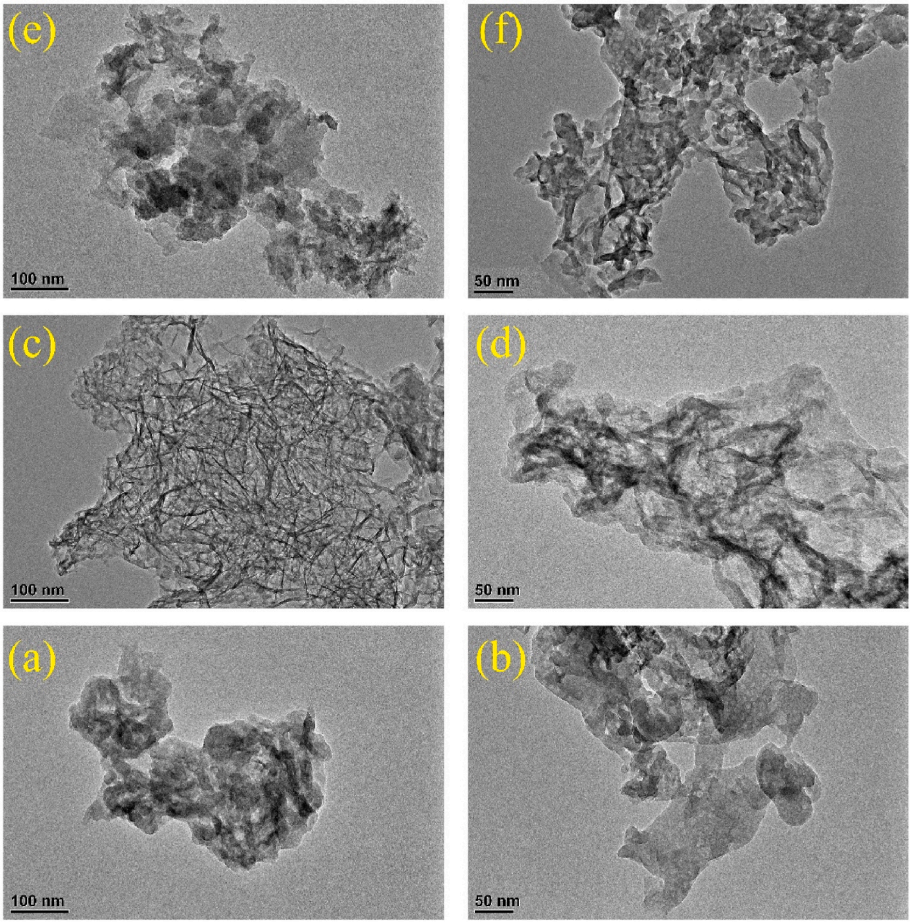

Fig. 4. TEM image of (a) Control CSH (100 nm), (b) Control CSH (50 nm), (c) L-Asp – CSH (100 nm), (d) L-Asp – CSH (50 nm), (e) PDA – CSH (100 nm), and (f) PDA - CSH (50 nm).

3.1.3. *Nanomechanical property of freshly prepared CSH*

The compacted CSH pellets were subjected to nanoindentation over two different 30 μm × 30 μm areas in a grid pattern resulting in a total of 120 indentations per sample. An example plot showing the load-depth graphs for different CSH samples is given in Figure S3. Based on the results from those 120 indentations, the frequency distribution of the elastic modulus of the pure CSH(control), PDA modified CSH, and L-Asp modified CSH are given in Fig. 5. The pure CSH was found to have a mean modulus of 3 GPa. This value exactly matches a recently reported measurement of a modulus of CSH with a C/S ratio of 1.0 [63]. PDA modified CSH showed a higher elastic modulus of 25 GPa which is around 8 times higher than the pure CSH. Worth noting, PDA is also well known for its adhesive properties [64]. The self-polymerization of dopamine hydrochloride to PDA in an alkaline environment creates a polymer network with strong adhesive properties [64]. We suggest that due to this adhesive nature, the PDA modification of CSH resulted in the observed increase in the modulus of CSH. The L-Asp modified CSH was found to have an elastic modulus of around 9 GPa which is around 3 times higher than the control sample. This increased modulus could be due to the formation of higher amounts of Q^3 as observed from the ^{29}Si NMR spectra. Considering the above results, it is interesting to note that the addition of biomimetic molecules can significantly enhance the elastic properties of CSH. These findings point toward a new approach for nano-engineering cement-based materials for superior mechanical performance. However, it is important to note that a previous study by Kamali and Ghahremaninezhad [48] reported that the modification of CSH by biomolecules reduced the elastic modulus of this phase. In that study [48], the used biomimetic molecules were arginine, leucine, glutamic acid, albumin, and hemoglobin. Therefore, the type of organic molecules used plays an important role in whether the elastic modulus of CSH is enhanced or not. Based on the current findings, it can be suggested that biomimetic molecules with distinct Ca^{2+} binding properties can enhance the modulus of CSH. However, additional investigations are required to confirm this observation.

3.2. *Effectiveness of biomimetic molecules to resist carbonation*

In the following sections, the characteristics of carbonated CSH are presented to evaluate the role of biomimetic molecules on the carbonation resistance of these samples.

3.2.1. *^{29}Si NMR spectra of carbonated samples*

The ^{29}Si NMR spectra of the 168 h and 28 days carbonated CSH samples are given in Fig. 6 (a) and (b), respectively. After 168 h of accelerated carbonation at a 4% CO_2 concentration, the pure CSH batch contained only Q^3 (around −100 ppm) and Q^4 (around −112 ppm) species. The complete absence of Q^1 and Q^2 species confirmed that the original CSH structure was fully deteriorated and had formed a highly polymerized 3-dimensional silica gel network. The NMR spectra for the control batch remained similar after 28 days of carbonation (contained only Q^3 and Q^4). Interestingly, in the case of the L-Asp and PDA modified batches, the original CSH structure containing Q^2 species were retained after 168 h of carbonation, and there was no Q^4 formation. After 28 days of carbonation, minor peaks corresponding to Q^3 and Q^4 species were observed, even though the intensities of Q^1 and Q^2 remained prominent. Accordingly, the PDA and L-Asp modifications were successful in

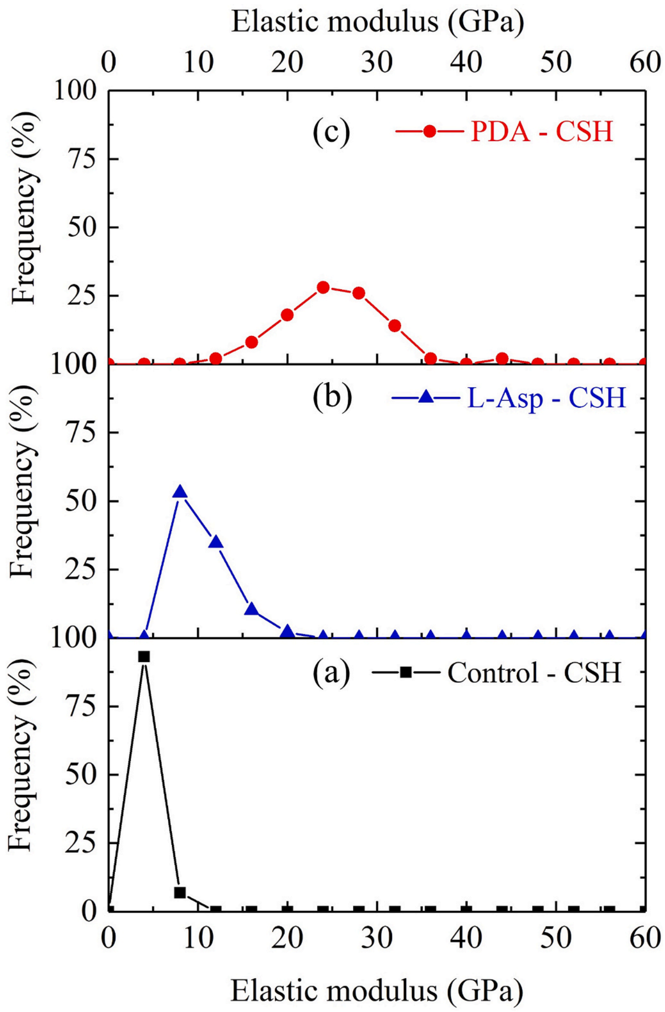

Fig. 5. Percent frequency vs elastic modulus of (a) pure CSH (b) L-Asp modified CSH, (c) PDA modified CSH without any carbonation.

significantly lowering the carbonation degradation of CSH. However, the chemical shift corresponding to Q^3 were in a lower range (- 90 to −100 ppm) for the modified CSH batches compared to those observed in the control batch (−104 ppm). This indicates the difference in the environment of the Q^3 species formed during the carbonation of CSH with and without the presence of biomimetic molecules and can correspond to the formation of organic-inorganic hybrid phases (CSH-organic molecule-$CaCO_3$) as hypothesized earlier.

3.2.2. *Nanostructure of CSH after carbonation*

The TEM images of the CSH samples after 168 h of carbonation are given in Fig. 7. In the case of the carbonated CSH batch, the presence of a crystalline phase within the disordered matrix is visible (Fig. 7(a)). This indicates the intermixing of $CaCO_3$ crystals in the carbonated CSH matrix. Such formation of a crystalline phase within the disordered matrix due to the carbonation of CSH has been reported in the past [65]. In the zoomed-in version (Fig. 7(b)), small globules with dense borders or periphery were observed. Such globules can be considered as the characteristic morphology of polymerized silica gel. In the case of PDA and L-Asp modified CSH, formation of such globules was not visible. It was observed that even after carbonation, the original foil-like morphology was retained for these batches, thus confirming other experimental observation that the biomimetic molecules modified CSH were able to retain the original molecular arrangements even after carbonation.

3.2.3. *FTIR spectra of CSH at different carbonation periods*

ATR-FTIR measurements has proven to be a highly valuable tool to monitor the polymerization of CSH [66] as well as the formation of various $CaCO_3$ polymorphs [40] during the carbonation reaction. In this work, FTIR spectra were collected from the carbonated CSH samples at certain intervals as shown in Fig. 8. The FTIR spectra for CSH exhibit a broad absorption between 800 cm^{-1} and 1200 cm^{-1} which corresponds to the asymmetrical stretching vibration (ν_3) of the Si–O bond present in silicate [66]. Based on the literature [67], the various polymerized silicate units in CSH were assigned as followings: the 960–980 cm^{-1} peaks are the Q^2 units, the 1050–1080 cm^{-1} peaks are the Q^3 units, and the 1100–1200 cm^{-1} are the Q^4 units. The $CaCO_3$ polymorphs can be identified by studying the asymmetrical stretching vibration (ν_3), the out-of-plane bending (ν_2), and the in-plane bending (ν_4) of the CO_3^{2-} bond in the ranges of 1300–1500 cm^{-1}, 800–900 cm^{-1} and 700–750 cm^{-1}, respectively [40,68].

With increased carbonation duration, the asymmetrical stretching vibration (ν_3) of CO_3^{2-} started forming at around 1420 cm^{-1} in the pure CSH sample (Fig. 8(a)). Additionally, sharp peaks at around 872 cm^{-1} and 711 cm^{-1} were also formed. These are characteristics peaks of calcite [40,69,70]. However, the minor peaks of out-of-plane bending at 858 cm^{-1} and in-plane bending at 700 cm^{-1} indicate the presence of a small amount of aragonite in the control batch after 168 h of

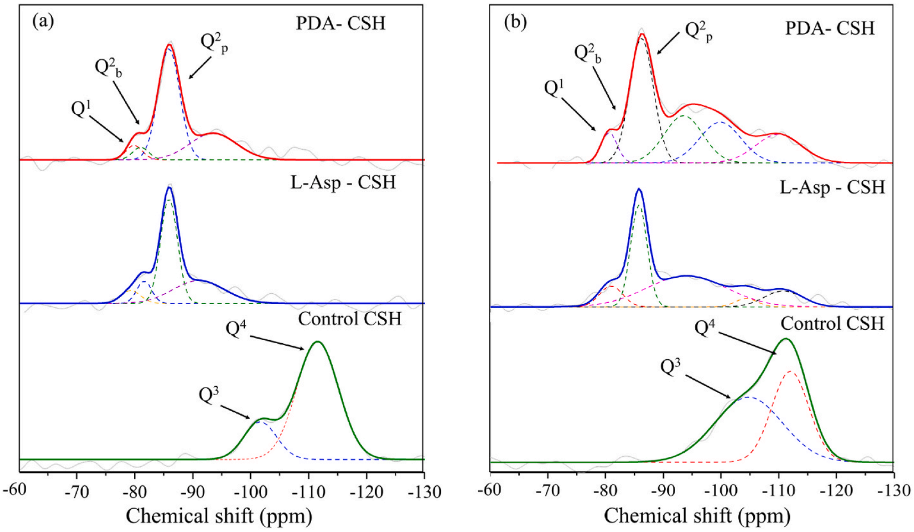

Fig. 6. ^{29}Si MAS NMR spectra of pure and modified CSH at (a) 168 h and (b) 28 days of carbonation.

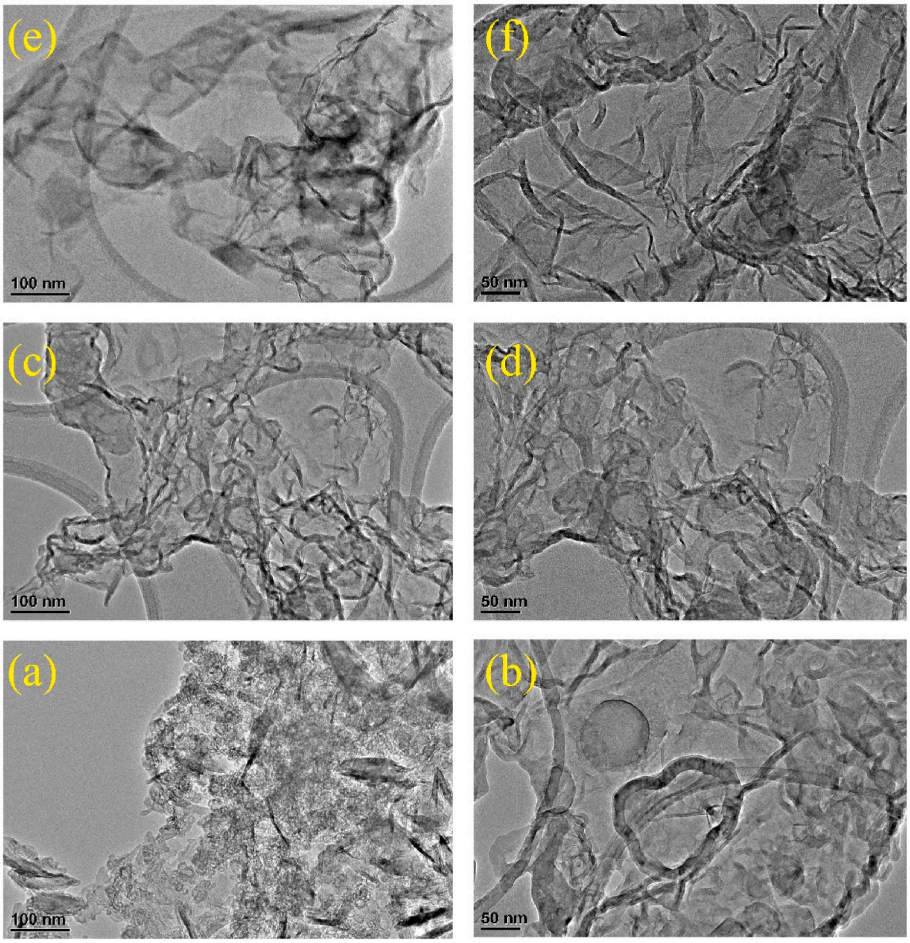

Fig. 7. TEM image of (a) pure CSH (100 nm), (b) pure CSH (50 nm), (c) L-Asp modified CSH (100 nm), (d) L-Asp modified CSH (50 nm), (e) PDA modified CSH (100 nm), and (f) PDA modified CSH (50 nm) after 168 h of carbonation period.

carbonation. Additionally, the in-plane bending peak at around 745 cm^{-1} also represents the formation of vaterite in these samples. Regardless, the characteristic peaks of calcite were most prominent in the control batch indicating that these samples primarily formed calcite but contained small amounts of vaterite and aragonite after 168 h of carbonation curing. The 28 days carbonated CSH samples also primarily contained the characteristic peaks for calcite (1410 cm^{-1}, 873 cm^{-1}, and 712 cm^{-1}). This indicates that the initially formed vaterite and aragonite were converted to stable calcite polymorph in the case of the pure CSH carbonated sample.

The FTIR spectra of the PDA modified, and L-Asp modified CSH samples before and after carbonation were very similar (Fig. 8(b) and (c)). Unlike the pure CSH sample, the asymmetrical stretching vibration (ν_3) of CO_3^{2-} bond started forming a split peak at around 1350 cm^{-1} and 1390 cm^{-1}. Such split peaks are the characteristic of ACC as well as vaterite [70,71]. The formation of out-of-plane and in-plane bending peaks at around 834 cm^{-1} and 744 cm^{-1}, respectively, in these samples also indicate the formation of vaterite in the biomimetic molecules modified CSH after carbonation. Unlikely the pure CSH samples, the characteristics FTIR peaks for ACC and vaterite were found to persist in the biomimetic-molecule modified CSH samples even after 28 days. Accordingly, it can be postulated that the presence of L-Asp and PDA stabilized the formation of ACC and vaterite in the carbonated CSH samples.

To understand the carbonation induced polymerization of CSH, the asymmetrical stretching vibration (ν_3) of the Si–O bond formed in the range of 900 cm^{-1} to 1200 cm^{-1} was analyzed. As observed in Fig. 8(a), the control batch initially had an asymmetrical stretching vibration (ν_3) of Si–O bond at around 960 cm^{-1} which is characteristic of the CSH structure. With increased carbonation duration, a peak at around 1100 cm^{-1}, corresponding to the Q^3 species, started forming. After 168 h of carbonation, the carbonated CSH sample contained primarily Q^3 and Q^4 peaks, in addition to Q^2 peaks. However, after 28 days of carbonation, only the absorption bands corresponding to Q^3 and Q^4 were visible, indicating the complete molecular arrangement of CSH was changed and formed a highly polymerized silica gel network. This observation also matches the finding of the ^{29}Si NMR spectra. In the case of the modified CSH samples, the original Q^2 structure of CSH was retained even after 28 days of carbonation, thus, corroborating the findings of ^{29}Si NMR, that the presence of biomimetic molecules was able to aid CSH in resisting carbonation-induced polymerization.

To obtain a semi-quantitative comparison, the FTIR absorption peak corresponding to the Si–O bond in the range of 900–1200 cm^{-1} was deconvoluted to get the mean wavenumber. The deconvolution method was presented in a previous publication [66], and one example plot showing the deconvolution is presented as supplementary data (Figure S4). The absorption bands below 900 cm^{-1} wavenumbers were not considered in the calculation to avoid the effect of the C–O bond which has an absorption band at around 870 cm^{-1}. The mean wavenumbers for the different CSH batches along with their carbonation durations are presented in Fig. 8(d). From this plot, it can be seen that the accelerated carbonation only slightly changed the chain silicate structure present in the L-Asp and PDA modified CSH samples. The original molecular arrangements of CSH were retained even after 28 days. However, in the case of the pure CSH sample, the conversion of CSH to the polymerized 3D network for silica gel happened within 168

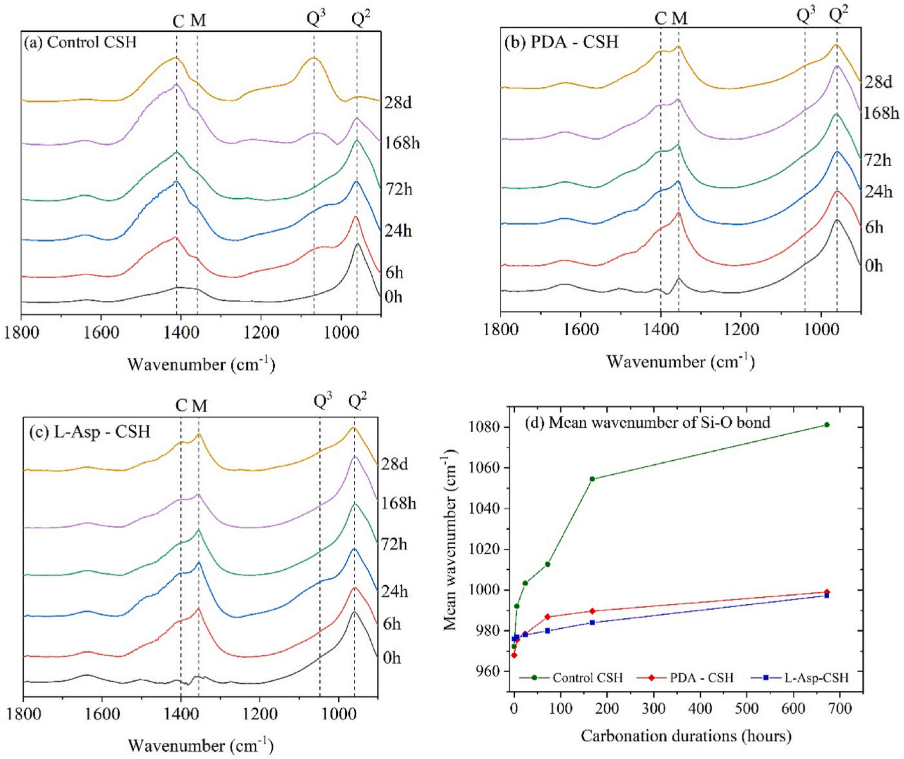

Fig. 8. FTIR spectra of (a) pure CSH; (b) PDA modified CSH; (c) L-Asp modified CSH at different carbonation periods [C: calcite and M: metastable calcium carbonate]; (d) mean wavenumber of the silica tetrahedron polymerization chain at different carbonation periods.

h.

3.2.4. Thermogravimetric analysis with mass spectroscopy (TGA-MS) for CO_2 sequestration capacity

The TGA-MS plots of CSH carbonated for 168 h and 28 days are presented in Figs. 9 and 10, respectively. Nearly all the CSH showed gradual weight loss due to the release of chemically bound water within the temperature range of 100 °C–600 °C, and the release of CO_2 due to the decarbonation of $CaCO_3$ within the temperature range of 200 °C–800 °C. As suggested previously, the gradual weight loss due to the decarbonation is primarily associated, including vaterite and ACC [40]. The decomposition (recrystallization to a stable phase) of ACC occurs in the temperature range of 170 °C–350 °C, depending on the particle size and pH [72,73]. In the case of vaterite, recrystallization

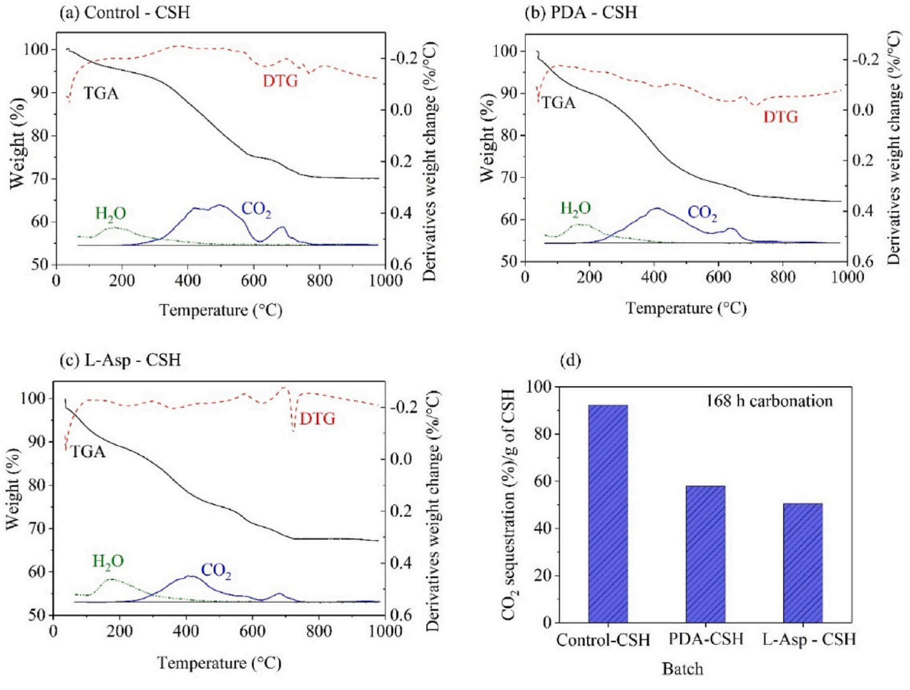

Fig. 9. Thermogravimetric analysis of CSH after 168 h of carbonation.

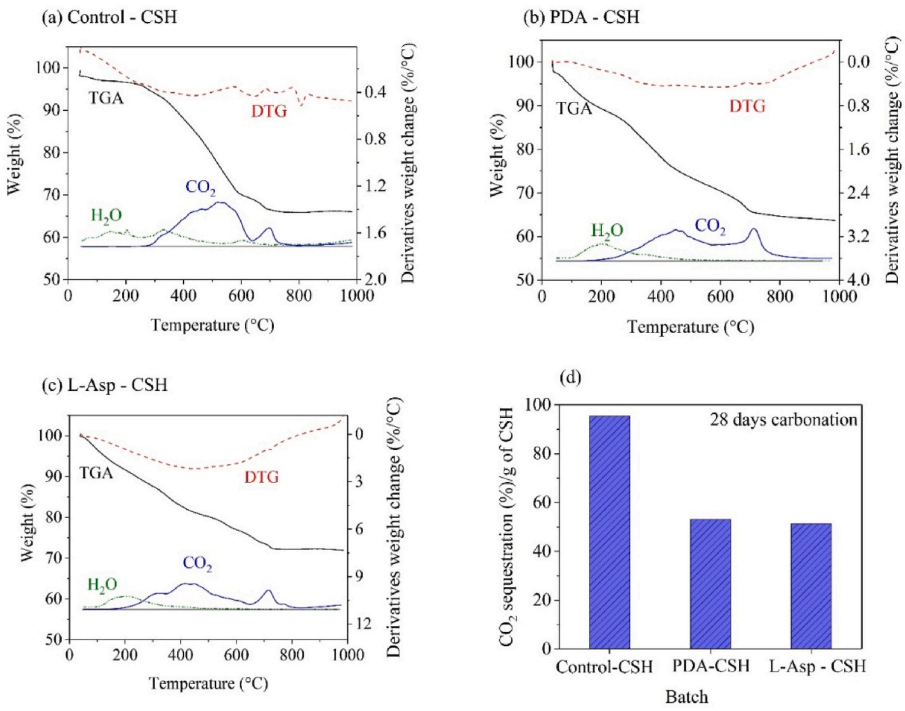

Fig. 10. Thermogravimetric analysis of CSH after 28 days of carbonation.

occurs at around 450 °C and exhibits multiple stages [74]. Based on this literature information, we mark four stages in the CO_2 mass spectra of the carbonated CSH samples and assign those stages as follows, I: recrystallization of ACC, II and III: recrystallization of vaterite, and IV: decomposition of calcite. Aragonite was not observed in these samples using XRD (see supplementary data). From Fig. 9(a), it can be observed that the carbonated control CSH contained vaterite, ACC, and calcite after 168 h of carbonation. The CO_2 spectra for L-Asp and PDA were similar to that of the control batch, except the intensity corresponding to vaterite was low. Based on the TGA-MS plots, the weight loss associated with the CO_2 release was further calculated and presented in Fig. 9(d). It can be observed that due to the carbonation, pure CSH was able to sequester around 20% CO_2. On the other hand, the CO_2 sequestration in the L-Asp and PDA modified CSH samples was around 11% and 15%, respectively. After 28 days of carbonation, the CO_2 release corresponding to ACC (stage I) was not observed in the control CSH batch [Fig. 10 (a)], but the intensity corresponding to vaterite was increased. In the case of the L-Asp modified CSH, after 28 days of carbonation, the intensity of CO_2 spectra corresponding to ACC was increased, whereas, in the case of the PDA modified CSH it remained the same as at 168 h. Accordingly, we suggest that while all the carbonated batches contained vaterite and calcite, only the biomimetic molecules modified batches produced a stable form of ACC. It was further observed that after 28 days of carbonation, the CO_2 sequestered in the control batch and PDA modified batch increased to 27% and 20%, respectively. On the other hand, the L-Asp modified CSH did not show any increase in CO_2 sequestration capacity after 28 days of carbonation. Accordingly, L-Asp modification was able to resist further carbonation of the samples after 168 h, and PDA modification slowed down the carbonation rate compared to that of the control batch. Interestingly, the biomimetic molecules modified CSH samples were able to sequester CO_2 without deteriorating the original chain like structure of the CSH.

3.2.5. *Nano-mechanical properties of carbonated samples*

The frequency distribution of the elastic modulus in the CSH pellets after 168 h and 28 days of carbonation are presented in Fig. 11(a) and Fig. 11(b), respectively. Considering the pure CSH batch, with an increased degree of carbonation, the average elastic modulus was observed to increase. This is expected considering calcite has a higher modulus compared to that of CSH. It is postulated that after 168 h of carbonation, the pure CSH pellets consist of $CaCO_3$ crystals, remaining original CSH, and polymerized silica gel. Considering the combination of these phases, the average elastic modulus was increased to around 15 GPa (original CSH average was 3 GPa). The average modulus remains close to the previously reported value for the carbonated compact CSH disc [63]. At this stage, the pure CSH also contained vaterite and ACC, which may have also resulted in a lower modulus compared to those of calcite. However, after 28 days of carbonation, the formation of calcite evidently caused a significant increase in the modulus. Interestingly, considering the frequency distribution of the elastic modulus, the presence of three distinct phases were clearly identifiable (as marked in Fig. 11(b)). This indicates that the carbonated pure CSH pellet contained a mixture of these three phases. In contrast, in the PDA modified CSH, the elastic modulus increased from 23 GPa to 36 GPa after 168 h of carbonation. Upon carbonation for 28 days, the average elastic modulus distribution shifted further to ~40 GPa. In the case of L-Asp modified CSH, this increase in elastic modulus was significantly more prominent. Specifically, L-Asp CSH had an average elastic modulus of 9 GPa before carbonation, which increased to 45 GPa after 168 h of carbonation. After 28 days of carbonation, the elastic modulus increased further to 55 GPa.

Worth noting, pure calcite crystals have an elastic modulus of around 60–70 GPa [76]. Therefore, the frequency distribution of the observed elastic modulus of the control batch can be statistically deconvoluted to three phases and assigned as follows: 20 GPa – remaining CSH and silica gel, 35 GPa – intermixed gel phase and calcite, and 65 GPa – calcite. In contrast, in the case of the PDA modified batch, there weren't any separable phases observed in the frequency distribution after 28 days of carbonation. Specifically, the frequency distribution appeared to have a normal distribution with mean modulus of around 36 GPa. A similar pattern was observed in the case of the L-Asp modified batch, except the mean modulus was higher (45–55 GPa). This observation further indicates the potential formation of a single hybrid phase, instead of separate microscopic phases (detailed discussion provided in sec 4).

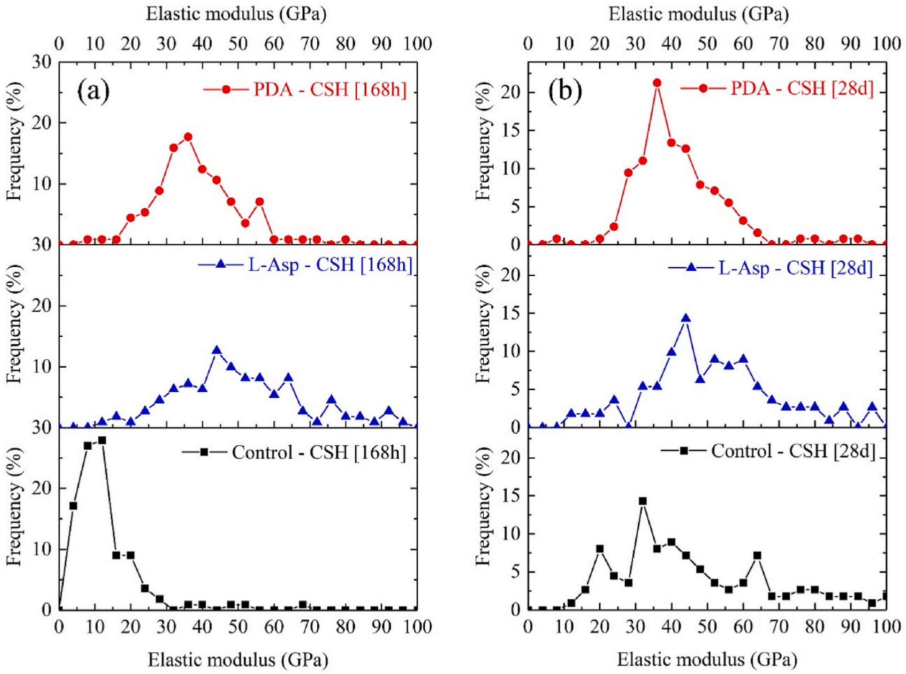

Fig. 11. Percent frequency vs elastic modulus of control CSH, PDA modified CSH, L-Asp modified CSH at (a) 168 h and (b) 28 days of carbonation.

3.2.6. *Morphologies of the $CaCO_3$ phases*

The morphologies of the $CaCO_3$ crystals formed in the carbonated CSH are shown in Fig. 12. Individual crystal sizes and shapes were visible in all the CSH batches [Fig. 12 (a to f)]. In the case of the control batch, $CaCO_3$ crystals were mostly embedded in the silica gel phase [Fig. 12 (a, b)]. However, sharp rhombohedral edges of calcite crystals were identifiable in the control batch. In contrast, in the cases of the L-Asp modified samples, spherical ACC were visible [Fig. 12 (c, d)]. On the other hand, PDA batches were found to contain vaterite plates. Based on the several SEM images, it was apparent that L-Asp and PDA primarily stabilized ACC and vaterite, respectively. However, both of the batches also found to contain some calcite crystals also (not shown in the figure).

4. Discussion and future applications

The primary finding of this study is that the carbonation-induced decalcification and subsequent polymerization of CSH can be reduced by biomimetic-molecule modifications. The enhanced carbonation resistance of CSH due to this modification can be attributed to the following mechanisms. The presence of the selected biomimetic molecules ensures the stabilization of ACC and vaterite during the early stages of carbonation of the CSH. The governing mechanism for how the molecules interact with the CSH is shown in Fig. 13. The negative surface sites from the biomimetic molecule gets attached with the positive Ca^{2+} from the CaO sheet of CSH and later forms the organic-inorganic hybrid phase during carbonation. The formation of organic-inorganic hybrid phase due to the presence of biomimetic molecules and $CaCO_3$ are discussed in a previous publication [40]. Specifically, it was suggested that during carbonation the negatively charged biomimetic molecules binds Ca^{2+} sites of $CaCO_3$ by sharing an electron [40]. Such a bond then inhibits further conversion of ACC and vaterite particles to calcite [40].

Stabilization of these metastable $CaCO_3$ polymorphs have multiple consequences:

(i) These polymorphs have lower solubility compared to that of calcite. Specifically, the solubility constants for calcite, aragonite, and vaterite are $10^{-8.48}$, $10^{-8.34}$, and $10^{-7.91}$, respectively [31, 32]. ACC is 120 times more soluble than calcite [33]. Due to the high solubility of ACC and vaterite, formation of these phases can reduce the extent of carbonation [22].

(ii) ACC (1.62–2.59 g/cc, depending on the H_2O content) and vaterite (2.66 g/cc) have lower density compared to that of calcite (2.71 g/cc) [77]. Accordingly, formation of same weight of metastable $CaCO_3$ occupies a higher volume compared to calcite, and therefore, formation of these $mCaCO_3$ reduces the CO_2 diffusion in the matrix.

(iii) As reported by Kim et al. [78], this approach of controlling the in-situ crystallization of $CaCO_3$ using biomimetic molecules results in the formation of organic-inorganic nanohybrids with superior elastic modulus and hardness compared to that of the pure calcite crystal.

We suggest that due to mechanisms (i) and (ii), the biomimetic molecule modified CSH showed notable resistance to the carbonation degradation compared to that of the pure CSH. In addition, the above mechanism (iii) is responsible for the increased modulus of elasticity of the modified CSH after carbonation. We further suggest that the biomimetic-molecule $CaCO_3$ was not the only hybrid phase, but rather a nanocomposite phase containing the CSH-biomimetic molecule-$mCaCO_3$ was formed which had excellent elastic modulus compared to the pure CSH. A brief comparison of Figs. 11 and 5 reveals that the elastic modulus of the above hybrid phase is 16 times higher than the pure CSH (a 49 GPa average modulus of carbonated L-Asp modified CSH vs. the 3 GPa of pure CSH).

The above findings can be highly beneficial for cementitious materials that contain CSH/CASH as the primary binding phases. These cementitious materials show degradation and strength loss due to carbonation-induced degradation of CSH. By utilizing the biomimetic molecules, it can be possible to reduce the carbonation degradation of the cementitious composites. Additionally, as observed due to the presence of biomimetic molecules, the mechanical properties of the CSH compacts were improved after carbonation. Thus, when the cementitious composites are exposed to atmospheric CO_2, the mechanisms of the biomimetic molecules will allow a denser outer layer to form which can work as an in-situ sealant layer for the composite.

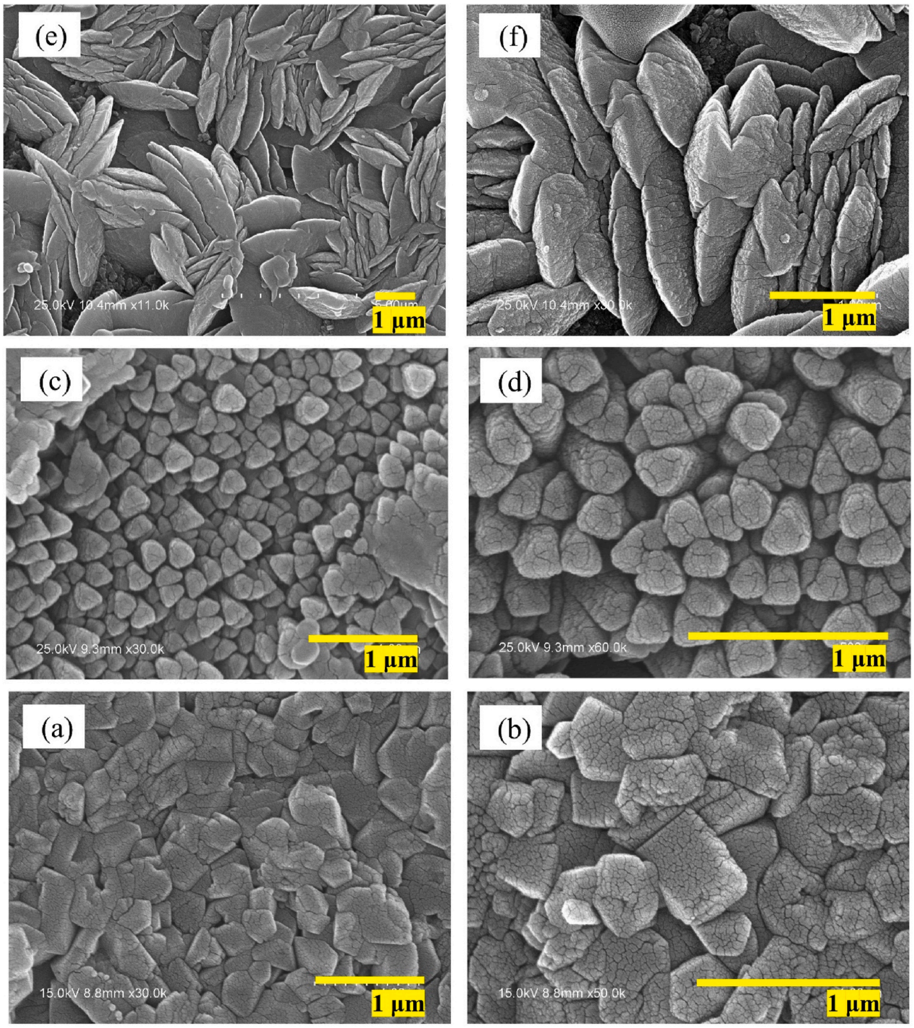

Fig. 12. SEM images showing the $CaCO_3$ morphology in carbonated (a and b) control; (c and d) L-Asp modified CSH; and (e and f) PDA modified CSH samples.

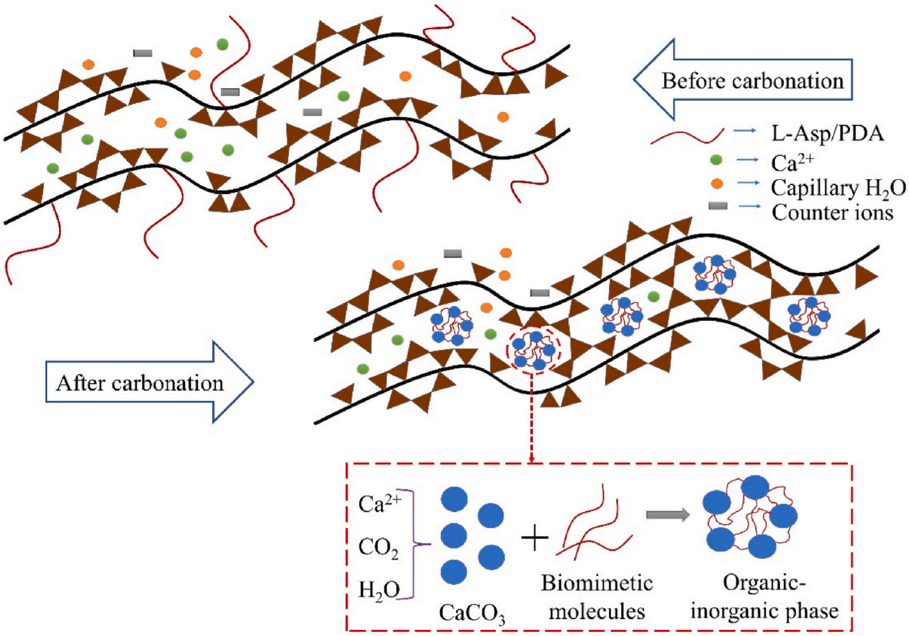

Fig. 13. Interaction of biomimetic molecules with the CSH and formation of organic-inorganic phase.

5. Conclusion

The following are the concluding remarks from the present study:

i. L-Asp and PDA-modified CSH showed foil-like morphology and similar silicate polymerization as that of the pure CSH. CSH modified with L-Asp and PDA had nearly 3 times and 8 times higher elastic modulus, respectively, compared to that of the pure CSH.
ii. From TEM image analysis, it was seen that the morphology of the modified CSH samples were unaffected even after 168 h carbonation duration. On the other hand, after 168 h of carbonation, pure CSH converted to spherical silica gel particles with distinguishable periphery.
iii. ^{29}Si NMR of the CSH samples before and after carbonation showed that within the carbonation duration, pure CSH was fully converted to polymerized silica gel containing Q^3 and Q^4 species. In the cases of L-Asp and PDA modified CSH, no significant change in the CSH polymerization was observed despite the increased amount of $CaCO_3$ formation after 28 days of carbonation.
iv. The modified CSH showed significantly increased elastic modulus after carbonation. The increase in the modulus of the L-Asp modified CSH batch was higher than that of the PDA modified CSH. The increase of modulus during carbonation was attributed to the formation of an organic-inorganic nanohybrid phase in the presence of the biomimetic molecules.
v. Under the tested experimental scenario, the modification by L-Asp and PDA reduced the CO_2 sequestration capacity of CSH by 45% and 25%, respectively. It is important to note that the result of this reduced CO_2 sequestration capacity was that the biomimetic-molecule modification allowed the CSH to retain its original structure and increased the elastic modulus after carbonation.

Overall, from this study, it was observed that the use of L-Asp and PDA could reduce the carbonation degradation of pure CSH. However, the effectiveness of such molecules for different C/S ratios and pH remains unexplored at this time and will require further investigation.

Declaration of competing interest

The authors declare that they have no known competing financial interests or personal relationships that could have appeared to influence the work reported in this paper.

Data availability

Data will be made available on request.

Acknowledgement

This work was conducted with funding support from the US National Science Foundation (NSF # ECI - 2028462). The TGA-MS measurements were collected using the IMSERC facilities at Northwestern University, which has received support from the Soft and Hybrid Nanotechnology Experimental (SHyNE) Resource (NSF ECCS-1542205), the State of Illinois, and the International Institute for Nanotechnology (IIN). All opinions, findings, and conclusions or recommendations expressed in this material are those of the authors and do not necessarily reflect the views of the funding agencies.

Appendix A. Supplementary data

Supplementary data to this article can be found online at https://doi.org/10.1016/j.cemconcomp.2022.104888.

References

[1] S. Huey, T. Wiedmann, A. Castel, J. De Burgh, Hybrid life cycle assessment of greenhouse gas emissions from cement , concrete and geopolymer concrete in Australia, J. Clean. Prod. 152 (2017) 312–320, https://doi.org/10.1016/j.jclepro.2017.03.122.

[2] C. Ouellet-Plamondon, G. Habert, Life cycle assessment (LCA) of alkali-activated cements and concretes, in: F. Pacheco-Torgal, J.A. Labrincha, C. Leonelli, A. Palomo, P. Chindaprasirt (Eds.), Handbook of Alkali-Activated Cements, Mortars and Concretes, Woodhead Publishing Limited, 2020, pp. 663–686, https://doi.org/10.1533/9781782422884.5.663.

[3] T. Bakharev, J.G. Sanjayan, Y.B. Cheng, Resistance of alkali-activated slag concrete to carbonation, Cement Concr. Res. 31 (2001) 1277–1283, https://doi.org/10.1016/S0008-8846(03)00125-X.

[4] F. Puertas, M. Palacios, T. Vázquez, Carbonation process of alkali-activated slag mortars, J. Mater. Sci. 41 (10) (2006) 3071–3082, https://doi.org/10.1007/s10853-005-1821-2.

[5] E. Gruyaert, P. Van den Heede, N. De Belie, Carbonation of slag concrete: effect of the cement replacement level and curing on the carbonation coefficient – effect of carbonation on the pore structure, Cem. Concr. Compos. 35 (1) (Jan. 2013) 39–48, https://doi.org/10.1016/j.cemconcomp.2012.08.024.

[6] A. Younsi, P. Turcry, A. Aït-Mokhtar, S. Staquet, Accelerated carbonation of concrete with high content of mineral additions: effect of interactions between hydration and drying, Cement Concr. Res. 43 (1) (2013) 25–33, https://doi.org/10.1016/j.cemconres.2012.10.008.

[7] B. Wu, G. Ye, Development of Porosity of Cement Paste Blended with Supplementary Cementitious Materials after Carbonation, vol. 145, 2017, pp. 52–61, https://doi.org/10.1016/j.conbuildmat.2017.03.176.

[8] M. Palacios, F. Puertas, Effect of carbonation on alkali-activated slag paste, J. Am. Ceram. Soc. 89 (10) (2006) 3211–3221, https://doi.org/10.1111/j.1551-2916.2006.01214.x.

[9] Z. Li, S. Li, Carbonation resistance of fly ash and blast furnace slag based geopolymer concrete, Construct. Build. Mater. 163 (2018) 668–680, https://doi.org/10.1016/j.conbuildmat.2017.12.127.

[10] V.G. Papadakis, M.N. Fardis, C.G. Vayenas, Hydration and carbonation of pozzolanic cements, ACI Mater. J. 89 (2) (1992), https://doi.org/10.14359/2185.

[11] M.Á. Sanjuán, E. Estévez, C. Argiz, D. del Barrio, Effect of curing time on granulated blast-furnace slag cement mortars carbonation, Cem. Concr. Compos. 90 (September 2017) (2018) 257–265, https://doi.org/10.1016/j.cemconcomp.2018.04.006.

[12] M. Sufian Badar, K. Kupwade-Patil, S.a. Bernal, J.L. Provis, E.N. Allouche, Corrosion of steel bars induced by accelerated carbonation in low and high calcium fly ash geopolymer concretes, Construct. Build. Mater. 61 (2014) 79–89, https://doi.org/10.1016/j.conbuildmat.2014.03.015.

[13] V. Shah, K. Scrivener, B. Bhattacharjee, S. Bishnoi, Changes in microstructure characteristics of cement paste on carbonation, Cement Concr. Res. 109 (April) (2018) 184–197, https://doi.org/10.1016/j.cemconres.2018.04.016.

[14] S.A. Bernal, The Resistance of Alkali-Activated Cement-Based Binders to Carbonation, Woodhead Publishing Limited, 2015, https://doi.org/10.1533/9781782422884.3.319.

[15] J.J. Chen, J.J. Thomas, H.M. Jennings, Decalcification shrinkage of cement paste 36 (2006) 801–809, https://doi.org/10.1016/j.cemconres.2005.11.003.

[16] T.C. Powers, A hypothesis on carbonation shrinkage, Journal of Portland Cement Association. Research and Development Laboratories 4 (2) (1962) 40–50.

[17] R. Liu, L. Jiang, J. Xu, C. Xiong, Z. Song, Influence of carbonation on chloride-induced reinforcement corrosion in simulated concrete pore solutions, Construct. Build. Mater. 56 (2014) 16–20, https://doi.org/10.1016/j.conbuildmat.2014.01.030.

[18] B. Huet, V. L'Hostis, F. Miserque, H. Idrissi, Electrochemical behavior of mild steel in concrete: influence of pH and carbonate content of concrete pore solution, Electrochim. Acta 51 (1) (2005) 172–180, https://doi.org/10.1016/j.electacta.2005.04.014.

[19] J.C. Walton, S. Bin-Shafique, R.W. Smith, N. Gutierrez, A. Tarquin, Role of carbonation in transient leaching of cementitious wasteforms, Environ. Sci. Technol. 31 (8) (1997) 2345–2349, https://doi.org/10.1021/es960964j.

[20] V.T. Ngala, C.L. Page, Effects of carbonation on pore structure and diffusional properties of hydrated cement pastes, Cement Concr. Res. 27 (7) (1997) 995–1007, https://doi.org/10.1016/S0008-8846(97)00102-6.

[21] S.E. P, Some results of the effect of carbonation on the porosity and pore size distribution of cement paste, Materials and Construction (1968) 521–526.

[22] A.E. Morandeau, C.E. White, Role of magnesium-stabilized amorphous calcium carbonate in mitigating the extent of carbonation in alkali-activated slag, Chem. Mater. 27 (19) (2015) 6625–6634, https://doi.org/10.1021/acs.chemmater.5b02382.

[23] S. Goto, K. Suenaga, T. Kado, Calcium silicate carbonation products, J. Am. Ceram. Soc. 78 (11) (1995) 2867–2872.

[24] G.W. Groves, A. Brough, I.G. Richardson, C.M. Dobson, Progressive changes in the structure of hardened C3S cement pastes due to carbonation, J. Am. Ceram. Soc. 74 (1991) 2891–2896, https://doi.org/10.1111/j.1151-2916.1991.tb06859.x.

[25] O. Shtepenko, C. Hills, A. Brough, M. Thomas, The effect of carbon dioxide on β-dicalcium silicate and Portland cement, Chem. Eng. J. 118 (1–2) (May 2006) 107–118, https://doi.org/10.1016/j.cej.2006.02.005.

[26] E.T. Stepkowska, M.A. Aviles, J.M. Blanes, GRADUAL TRANSFORMATION OF Ca (OH) 2 INTO CaCO 3 ON CEMENT HYDRATION XRD study, Journal ofThermal Analysis and Calorimetry 87 (2007) 189–198.

[27] R. Ylmén, U. Jäglid, Carbonation of Portland cement studied by diffuse reflection fourier transform infrared spectroscopy, Int J Concr Struct Mater 7 (2) (May 2013) 119–125, https://doi.org/10.1007/s40069-013-0039-y.

[28] P. López-Arce, L.S. Gómez-Villalba, S. Martínez-Ramírez, M. Álvarez de Buergo, R. Fort, Influence of relative humidity on the carbonation of calcium hydroxide nanoparticles and the formation of calcium carbonate polymorphs, Powder Technol. 205 (1–3) (2011) 263–269, https://doi.org/10.1016/j.powtec.2010.09.026.

[29] S. Goñi, M.T. Gaztañaga, a. Guerrero, Role of cement type on carbonation attack, J. Mater. Res. 17 (2002) 1834–1842, https://doi.org/10.1557/JMR.2002.0271, 07.

[30] D. Gebauer, A. Völkel, H. Cölfen, Stable prenucleation calcium carbonate clusters, Science 322 (5909) (1979) 1819–1822, https://doi.org/10.1126/science.1164271, 2008.

[31] L.N. Plummer, E. Busenberg, The solubilities of calcite, aragonite and vaterite in CO2, Geochem. Cosmochim. Acta 46 (6) (1982) 1011–1040, https://doi.org/10.1016/0016-7037(82)90056-4.

[32] D. Ren, Q. Feng, X. Bourrat, Effects of additives and templates on calcium carbonate mineralization in vitro, Micron 42 (3) (2011) 228–245, https://doi.org/10.1016/j.micron.2010.09.005.

[33] O.E. Meiron, et al., Solubility and bioavailability of stabilized amorphous calcium carbonate, J. Bone Miner. Res. 26 (2) (2011) 364–372, https://doi.org/10.1002/jbmr.196.

[34] S.Y. Wang, E. McCaslin, C.E. White, Effects of magnesium content and carbonation on the multiscale pore structure of alkali-activated slags, Cement Concr. Res. 130 (October 2019) (2020), 105979, https://doi.org/10.1016/j.cemconres.2020.105979.

[35] N.A.J.M. Sommerdijk, G. De With, Biomimetic CaCO 3 mineralization using designer molecules and interfaces, Chem. Rev. 108 (11) (2008) 4499–4550.

[36] J.H.E. Cartwright, A.G. Checa, J.D. Gale, D. Gebauer, C.I. Sainz-díaz, Calcium carbonate polyamorphism and its role in biomineralization: how many amorphous calcium carbonates are there? Angew. Chem. Int. Ed. 51 (48) (2012) 11960–11970, https://doi.org/10.1002/anie.201203125.

[37] K. Maruyama, T. Yoshino, H. Kagi, Synthesizing a composite material of amorphous calcium carbonate and aspartic acid, Mater. Lett. 65 (2) (2011) 179–181, https://doi.org/10.1016/j.matlet.2010.09.039.

[38] Z. Zou, L. Bertinetti, Y. Politi, P. Fratzl, W.J.E.M. Habraken, Control of polymorph selection in amorphous calcium carbonate crystallization by poly(aspartic acid): two different mechanisms, Small 13 (21) (2017) 1–11, https://doi.org/10.1002/smll.201603100.

[39] P. Stempfle, O. Pantale, R.K. Njiwa, M. Rousseau, E. Lopez, X. Bourrat, Friction-induced sheet nacre fracture: effects of nano-shocks on cracks location, Int. J. Nanotechnol. 4 (6) (2015) 712, https://doi.org/10.1504/ijnt.2007.015466.

[40] R.I. Khan, W. Ashraf, J. Olek, Amino acids as performance-controlling additives in carbonation-activated cementitious materials, Cement Concr. Res. 147 (2021), https://doi.org/10.1016/j.cemconres.2021.106501.

[41] S. Kim, C.B. Park, Dopamine-induced mineralization of calcium carbonate vaterite microspheres, Langmuir 26 (21) (2010) 14730–14736, https://doi.org/10.1021/la1027509.

[42] S.S. Wang, A.W. Xu, Amorphous calcium carbonate stabilized by a flexible biomimetic polymer inspired by marine mussels, Cryst. Growth Des. 13 (5) (2013) 1937–1942, https://doi.org/10.1021/cg301759t.

[43] Z. Li, B. Peng, Z. Deng, Biomimetic synthesis of calcium carbonate films on bioinspired polydopamine matrices, J. Coating Technol. Res. 14 (5) (2017) 1095–1105, https://doi.org/10.1007/s11998-016-9898-x.

[44] Z. Liu, et al., Effect of polydopamine on the biomimetic mineralization of mussel-inspired calcium phosphate cement in vitro, Mater. Sci. Eng. C 44 (2014) 44–51, https://doi.org/10.1016/j.msec.2014.07.063.

[46] Y. Fang, J. Wang, X. Qian, L. Wang, G. Lin, Z. Liu, Bio-inspired functionalization of very fine aggregates for better performance of cementitious materials, Construct. Build. Mater. 241 (2020), 118104, https://doi.org/10.1016/j.conbuildmat.2020.118104.

[47] A. Picker, L. Nicoleau, A. Nonat, C. Labbez, H. Cölfen, Identifi Cation of Binding Peptides on Calcium Silicate Hydrate : A Novel View on Cement Additives, 2014, pp. 1135–1140, https://doi.org/10.1002/adma.201303345.

[48] M. Kamali, A. Ghahremaninezhad, Effect of Biomolecules on the Nanostructure and Nanomechanical Property of, 2018, pp. 1–16, https://doi.org/10.1038/s41598-018-27746-x, no. June.

[49] H. Matsuyama, J.F. Young, Synthesis of calcium silicate hydrate/polymer complexes : Part II . Cationic polymers and complex formation with different polymers, J. Mater. Res. 14 (8) (1999) 3389–3396.

[50] H. Matsuyama, J.F. Young, Synthesis of calcium silicate hydrate/polymer complexes : Part I. Anionic and nonionic polymers, J. Mater. Res. 14 (8) (1999) 3379–3388.

[54] C.T. Kao, et al., Surface modification of calcium silicate via mussel-inspired polydopamine and effective adsorption of extracellular matrix to promote osteogenesis differentiation for bone tissue engineering, Materials 11 (9) (2018), https://doi.org/10.3390/ma11091664.

[55] R.I. Khan, M.I. Haque, W. Ashraf, S. Shah, N. Saleh, Role of biopolymers in enhancing multiscale characteristics of carbonation-cured cementitious composites, Cement Concr. Compos. 134 (2022), https://doi.org/10.1016/J.CEMCONCOMP.2022.104766, 104766, doi:.

[56] W. Ashraf, J. Olek, N. Tian, Multiscale characterization of carbonated wollastonite paste and application of homogenization schemes to predict its effective elastic modulus, Cem. Concr. Compos. 72 (2016) 284–298, https://doi.org/10.1016/j.cemconcomp.2016.05.023.

[57] W.C. Oliver, G.M. Pharr, An improved technique for determining hardness and elastic-modulus using load and displacement sensing indentation experiments, J. Mater. Res. 7 (6) (1992) 1564–1583, 10.1557/.

[58] I.G. Richardson, Nature of CSH in hardened cements, Cement Concr. Res. 29 (8) (1999), https://doi.org/10.1016/S0008-8846(99)00168-4.

[59] H. Lechert, G. Engelhardt und, D. Michel, High Resolution Solid State NMR of Silicates and Zeolites, vol. 485, John Wiley & Sons, Chichester, New York, Brisbane, Toronto, Singapore, 1987, https://doi.org/10.1002/bbpc.198800267. Seiten, Preis: $ 55.-. ,” Berichte der Bunsengesellschaft für physikalische Chemie, vol. 92, no. 9, 1988.

[60] T.F. Sevelsted, J. Skibsted, Carbonation of C–S–H and C–A–S–H samples studied by 13C, 27Al and 29Si MAS NMR spectroscopy, Cement Concr. Res. 71 (2015) 56–65, https://doi.org/10.1016/j.cemconres.2015.01.019.

[61] X. Cong, R.J. Kirkpatrick, 29Si MAS NMR study of the structure of calcium silicate hydrate, Adv. Cement Base Mater. 3 (96) (1996) 144–156, https://doi.org/10.1016/S1065-7355(96)90046-2.

[62] M. Schönlein, J. Plank, A TEM study on the very early crystallization of CSH in the presence of polycarboxylate superplasticizers : transformation from initial CSH globules to nanofoils, Cement Concr. Res. 106 (June 2017) (2018) 33–39, https://doi.org/10.1016/j.cemconres.2018.01.017.

[63] R. Hay, J. Li, K. Celik, Phase evolution, micromechanical properties , and morphology of calcium (alumino) silicate hydrates C-(A-) S-H under carbonation, Cement Concr. Res. 152 (November 2021) (2022), 106683, https://doi.org/10.1016/j.cemconres.2021.106683.

[64] Z. Liu, et al., Effect of polydopamine on the biomimetic mineralization of mussel-inspired calcium phosphate cement in vitro, Mater. Sci. Eng. C 44 (2014) 44–51, https://doi.org/10.1016/j.msec.2014.07.063.

[65] V. Morales-Florez, N. Findling, F. Brunet, Changes on the nanostructure of cementitius calcium silicate hydrates (C–S–H) induced by aqueous carbonation, J. Mater. Sci. 47 (2) (Aug. 2011) 764–771, https://doi.org/10.1007/s10853-011-5852-6.

[66] W. Ashraf, J. Olek, Carbonation behavior of hydraulic and non-hydraulic calcium silicates: potential of utilizing low-lime calcium silicates in cement-based materials, J. Mater. Sci. 51 (13) (2016) 6173–6191, https://doi.org/10.1007/s10853-016-9909-4.

[67] N.Y. Mostafa, A.A. Shaltout, H. Omar, S.A. Abo-el-enein, Hydrothermal Synthesis and Characterization of Aluminium and Sulfate Substituted 1 . 1 Nm Tobermorites, vol. 467, 2009, pp. 332–337, https://doi.org/10.1016/j.jallcom.2007.11.130.

[68] P. Yin, IR - Spectroscopic Investigations of the Kinetics of Calcium Carbonate Precipitation, 2016.

[69] N. V Vagenas, A. Gatsouli, C.G. Kontoyannis, Quantitative analysis of synthetic calcium carbonate polymorphs using FT-IR spectroscopy, Talanta 59 (2003) 831–836, https://doi.org/10.1016/S0039-9140(02)00638-0.

[70] P. Yin, IR - Spectroscopic Investigations of the Kinetics of Calcium Carbonate Precipitation, 2016.

[71] F.a. Andersen, L. Brečević, Infrared spectra of amorphous and crystalline calcium carbonate, Acta Chem. Scand. 45 (1991) 1018–1024, https://doi.org/10.3891/acta.chem.scand.45-1018.

[72] N. Koga, Y. Nakagoe, H. Tanaka, Crystallization of amorphous calcium carbonate, Thermochim. Acta 318 (September 1997) (1998) 239–244.

[73] Z. Zou, et al., Opposite particle size E ff ect on amorphous calcium carbonate crystallization in water and during heating in air, Chem. Mater. 27 (2015) 4237–4246, https://doi.org/10.1021/acs.chemmater.5b00145.

[74] N. Nassrallah-Aboukaïs, C. Jacquemin, J. Decarne, E. Abi-Aad, J.F. Lamonier, A. Aboukaïs, Transformation of vaterite into calcite in the absence and the presence of copper (II) species . Thermal analysis , IR and EPR study E, J. Therm. Anal. Calorim. 74 (1) (2003) 21–27.

[76] W. Ashraf, J. Olek, N. Tian, Nanomechanical characterization of the carbonated wollastonite system, Nanotechnology in Construction (2015), https://doi.org/10.1007/978-3-319-17088-6_8.

[77] M. Saharay, A.O. Yazaydin, R.J. Kirkpatrick, Dehydration-induced amorphous phases of calcium carbonate, J. Phys. Chem. B 117 (12) (2013) 3328–3336, https://doi.org/10.1021/jp308353t.

[78] Y.Y. Kim, et al., Tuning hardness in calcite by incorporation of amino acids, Nat. Mater. 15 (8) (2016) 903–910, https://doi.org/10.1038/nmat4631.

Further reading

[45] Z. Liu, et al., Effect of polydopamine on the biomimetic mineralization of mussel-inspired calcium phosphate cement in vitro, Mater. Sci. Eng. C 44 (2014) 44–51, https://doi.org/10.1016/j.msec.2014.07.063.

[51] H. Matsuyama, J.F. Young, Synthesis of calcium silicate hydrate/polymer complexes : Part II . Cationic polymers and complex formation with different polymers, J. Mater. Res. 14 (8) (1999) 3389–3396.

[52] H. Matsuyama, J.F. Young, Synthesis of calcium silicate hydrate/polymer complexes : Part I. Anionic and nonionic polymers, J. Mater. Res. 14 (8) (1999) 3379–3388.

[53] Y. Fang, J. Wang, X. Qian, L. Wang, G. Lin, Z. Liu, Bio-inspired functionalization of very fine aggregates for better performance of cementitious materials, Construct. Build. Mater. 241 (2020), 118104, https://doi.org/10.1016/j.conbuildmat.2020.118104.

[75] R. Hay, J. Li, K. Celik, Phase evolution, micromechanical properties , and morphology of calcium (alumino) silicate hydrates C-(A-) S-H under carbonation, Cement Concr. Res. 152 (November 2021) (2022), 106683, https://doi.org/10.1016/j.cemconres.2021.106683.